RESEARCH ARTICLE

NANO · MICRO small
www.small-journal.com

Alloying of Mn with Bi-Rich Surfaces of Bi_2Te_3 by Topotactic Reaction

*Salma Khatun, Nikhilesh Maity, Sergey Lisenkov, Inna Ponomareva, and Matthias Batzill**

Interfacing topological insulators (TI) with magnetic materials enables accessing quantum effects for advanced devices. The synthesis of such heterostructures faces challenges due to interlaying mixing and the often-complex multicomponent materials required to combine the desired properties. An alternative synthesis to direct growth is the modification of 2D materials by topotactic reactions to introduce new functionalities into pre-formed single or few-component 2D sheets. Here, the self-formation of bismuthene (a bilayer of Bi; Bi_2) is utilized by thermal decomposition of Bi_2Te_3 as a platform to create novel 2D overlayers on the TI- substrate. Specifically, the Bi_2 layer is modified by reacting it with vapor deposited Mn in an attempt to induce magnetic properties. Scanning tunneling microscopy indicates that the Mn modified surface remains in a planar 2D layer, indicating the formation of an ordered Mn-rich surface layer. Density functional theory (DFT) is used to develop models of both the Bi-rich Bi_2Te_3 surface as well as their subsequent Mn-modified structure. The DFT models indicate the possibility of magnetic ordering of the high spin Mn^{2+} ions. The successful synthesis of planar MnBi alloys on a van der Waals material illustrates topotactic reactions as an alternative for creating novel layered heterostructures.

1. Introduction

Magnetism in topological materials may support novel quantum phenomena like Majorana fermions, quantum anomalous Hall effect (QAHE), axion insulator state, quantized magnetoelectric effect, and so forth.[1–3] Dilute doping with magnetic elements was the initial approach to incorporate magnetism in topological materials,[4,5] although the random distribution of dopants creates controversies regarding the breaking of time-reversal symmetry.[6] Another approach is to induce magnetism in topological insulators (TIs) by proximity with a 2D van der Waals (vdW) ferromagnet. For example, in the $Cr_2Ge_2Te_6/(Bi,Sb)_2Te_3$ heterostructure the anomalous Hall effect was observed by magnetic proximity-induced magnetism.[7] Such heterostructures are, however, challenging to synthesize and often rely on mechanical exfoliation and stacking of vdW materials. Direct modification of the surfaces of TIs with a magnetic layer is an alternative approach for the formation of van der Waals heterostructures with desirable properties. In previous studies, we have demonstrated that the surface reaction of Bi_2Se_3 with Mn results in the topotaxy of $MnBi_2Se_4$,[8] a known ferromagnetic vdW material. In addition, topotactical surface reactions in vdW materials have also been demonstrated to result in other 2D or pseudo 2D materials[9–11] and thus is a promising general method for modifying and inducing new properties, such as magnetism, into surface layers.

Here we focus on formation of potentially magnetic overlayers on Bi_2Te_3 by topotactical reaction with Mn. At first sight, a similar reaction as for Bi_2Se_3[8] and formation of the thermodynamically stable $MnBi_2Te_4$ compound may be anticipated. But the formation of $MnBi_2Te_4$ competes with other Mn-Te phases and this prevents the topotactical formation of $MnBi_2Te_4$ in this case. Specifically, we show that deposition of Mn on pristine Bi_2Te_3 results in the formation of Mn-telluride and a Bi-rich surface rather than the formation of the more desirable $MnBi_2Te_4$ phase. On the other hand, thermal evaporation of Te by vacuum annealing is well documented to result in Bi-rich surface layer, generally assumed to consist of bismuthene layers (bi-layer of Bi). The Bi_2/Bi_2Te_3 heterolayer structure has also been observed experimentally for bulk materials forming various compounds made up of bismuth (Bi_2)- and Bi_2Te_3- layers.[12] Also, due to the analogous layered structure and negligible lattice mismatch, Bi_2Te_3 has been used as a substrate for the MBE growth of Bi_2 layers with an atomically sharp interface.[13] Previous reports have shown Bi_2 island formation when annealing the Bi_2Te_3 thin films due to the thermal desorption of tellurium atoms.[14,15] Such a self-formation of a Bi-rich surface opens opportunities for its modification by Mn to form an ordered surface alloy, with the prospect for the formation of magnetic layers. Reaction of Mn with a Bi_2 layer on top of a Bi_2Te_3 crystal has the potential for the formation of a MnBi alloy. MnBi is a binary alloy that is one of the candidates for a rare-earth element-free permanent magnet.[16,17] It has two types of phases α-MnBi and β-MnBi.[16] The α-MnBi phase, also called the low-temperature phase (LTP), crystallizes in the hexagonal NiAs -structure and has ferromagnetic properties.[16,18] Some melting and casting routes,

S. Khatun, N. Maity, S. Lisenkov, I. Ponomareva, M. Batzill
Department of Physics
University of South Florida
Tampa, FL 33620, USA
E-mail: mbatzill@usf.edu

The ORCID identification number(s) for the author(s) of this article can be found under https://doi.org/10.1002/smll.202504498

DOI: 10.1002/smll.202504498

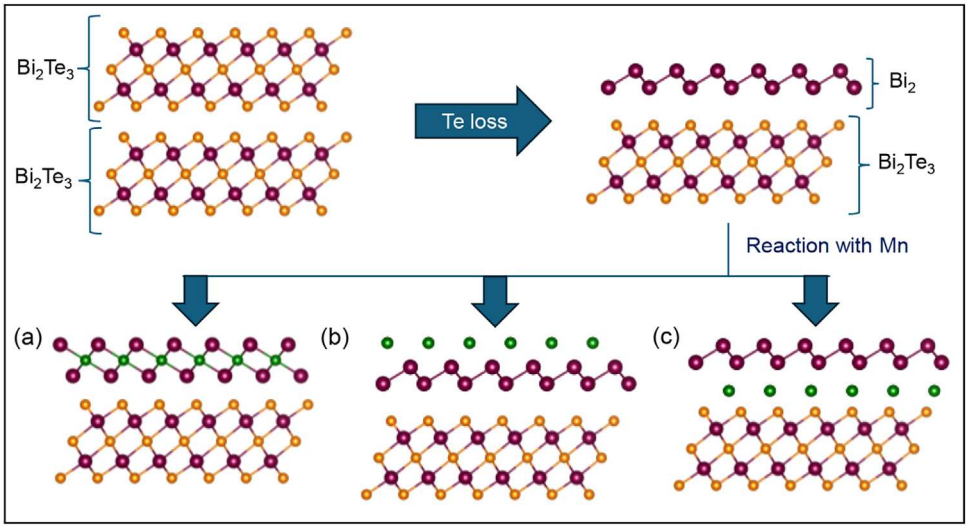

Figure 1. Schematic representation of the two-step reaction process. First, the Bi_2 layer is formed by the thermal desorption of Te-atoms. In the second step, the Bi_2 layer is reacted with Mn. Three possible ways of Mn addition are illustrated. a) Mn is inserted between Bi-layers to form the desired Mn_xBi_y phase, b) Mn atoms bind with the top surface atoms, and c) Mn atoms intercalate between the surface Bi_2 and Bi_2Te_3 layers.

arc melting, induction melting, zone melting, and directional solidification, are used to grow MnBi bulk samples.[19] Recently, large linear non-saturating magnetoresistance and high mobility have been observed in single-crystal ferromagnetic MnBi.[20] Several studies have also focused on preparing MnBi thin films as they have diverse advantages over bulk materials and can be incorporated into modern applications. Different types of physical vapor deposition methods, for instance, electron beam evaporation, pulsed laser deposition, and magnetron sputtering have been used to grow MnBi thin films.[21–23]

In this study, we investigated the reaction of Mn with Bi-rich Bi_2Te_3 surfaces. The bismuthene surface layer provides a natural 2D structure, and we find that the reaction with Mn maintains this layered structure, thus pointing toward the formation of a (pseudo) 2D heterostructure on top of a Bi_2Te_3 substrate. Potential alloy structures and their magnetic properties are investigated by density functional theory (DFT) which suggests that the high-spin state of Mn may order ferromagnetically. Thus the achieved 2D morphology as well as potential desirable magnetic ordering make the surface reaction of bismuthene with Mn an exciting system for adding magnetic adlayers to Bi_2Te_3.

2. Results and Discussion

The topotactic reaction steps are shown schematically in **Figure 1**. Initially, we formed a Bi-rich layer on the surface by thermally desorbing Te and subsequently reacting this surface with vapor-deposited Mn. There are various ways in which Mn can be added to Bi_2 layers. We have shown three possible reaction pathways for Mn incorporation. It can reside between two bismuth atomic layers and form the desired Mn_xBi_y phase (Figure 1a), Mn atoms can bind with top surface atoms (Figure 1b), and it can intercalate between the Bi_2 and Bi_2Te_3 layers.

We have used scanning tunneling microscopy (STM) to scrutinize the evolution of surface morphology, and X-ray photoelectron spectroscopy has been used to get the chemical state information of the elements. The stability of different phases and their magnetic ordering has been evaluated by the first-principles DFT calculations.

2.1. Evolution of Surface Morphology of Bi_2Te_3 Single Crystal with Annealing

The Bi_2Te_3 single crystals are exfoliated in air, transferred to a UHV chamber, and degassed for a few hours at 15 °C to get a clean surface. The large-scale STM topography shows some randomly shaped pits with a depth ranging from 0.1 to 0.3 nm, as shown in **Figure 2**a. The inset shows a hexagonal atomically resolved image of the Bi_2Te_3 surface. Terrace heights corresponding to a quintuple-layer, i.e., Te-Bi-Te-Bi-Te, (QL) thickness (≈1 nm) are observed on the surface up to annealing temperatures of 200 °C. After annealing to 200 ° C triangular-shaped holes are observed, which are also present at the edges of the Bi_2Te_3 layers. The depth of the holes is 1 nm, which is the same as 1 QL, as shown in Figure 2b. The separation between terraces suggests that the surface maintains a Bi_2Te_3 structure and composition for annealing temperatures up to 200 °C. The surface structure changed significantly after annealing to 300 °C. Islands with a thickness of 0.4 nm and meandering step edges are formed on the surface, as presented in Figure 2c. The layer in between these islands has a different morphology than the islands. Specifically, the surface is covered with a high density of ≈0.2 nm deep and 1–2 nm wide holes. Figure S1 (Supporting Information) shows the morphology of these terraces in higher resolution. Thermal desorption of tellurium atoms is a familiar process in telluride-based samples when annealed to 300 °C or higher. The experimental results are supported by DFT studies that showed Te to be nearly twice as volatile as Bi, as shown in Figure S3 (Supporting Information). Bismuth bilayer or bismuthene is a stable 2D material that can be grown, for instance, via molecular beam epitaxy.[24] It is also observed that a bismuth

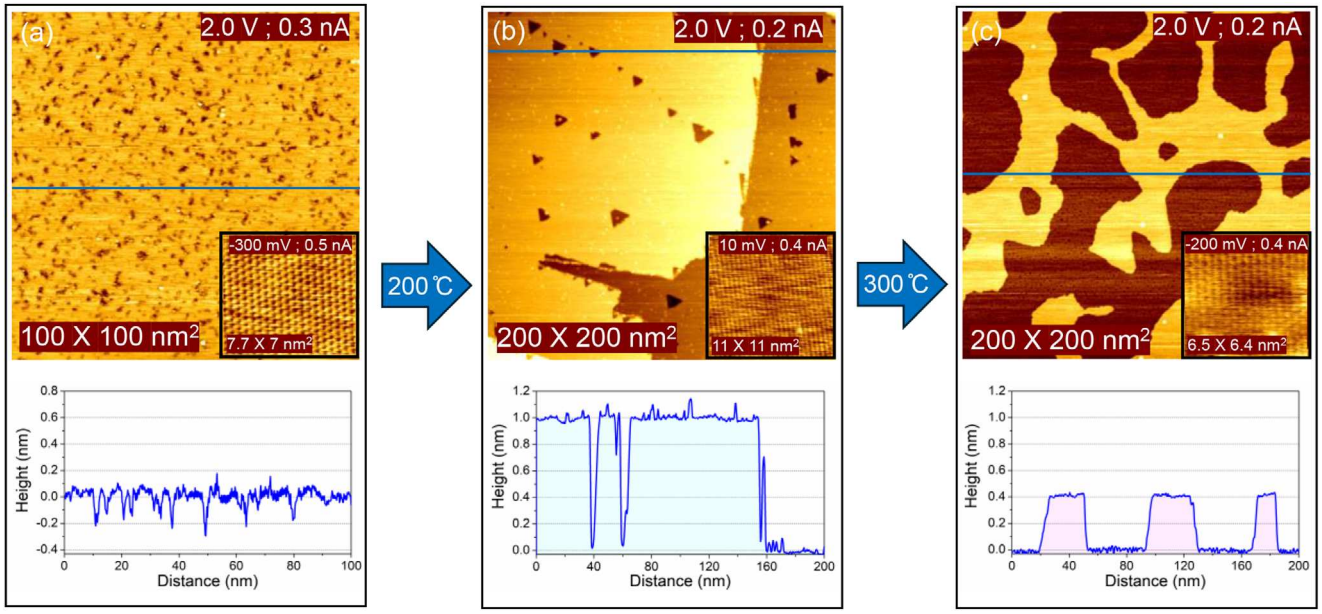

Figure 2. STM images of the Bi_2Te_3 single crystal after annealing to different temperatures. a) A large-scale STM image shows the surface of a Bi_2Te_3 crystal after annealing at 150 °C. Some small dips of random shape and size are located throughout the surface. The depth of these defects varies from 0.1 to 0.3 nm. The atomically resolved image in the inset shows a hexagonal pattern of Bi_2Te_3. b) After annealing the sample to 200 °C, triangular-shaped 1 nm deep holes formed. The depth is the same as the thickness of 1 quintuple layer of Bi_2Te_3. These triangular or half-triangular holes are also observed at the edges. c) The surface morphology changed when annealed at 300 °C. Irregular shaped islands of thickness 0.4 nm are observed that are consistent with the formation of bismuthene ad-islands.

bilayer formed on the surface of Bi_2Te_3 thin films when annealed to a high temperature.[14,15] The evolution of Bi-4f and Te-3d core level spectra with different annealing temperatures is shown in Figure S2 (Supporting Information). The Te-3d peak position remains the same, but there is a ≈ 0.1 eV shift toward lower binding energy for the Bi-4f peak after annealing at 300 °C, as shown in Table S1 (Supporting Information). The shift also suggests the presence of a bismuth-rich compound. Based on these previous observations and the fact that a 0.4 nm step height corresponds closely to the layer height of bismuthene we conclude that the meandering islands are likely Bi_2 layers. The fact that the lower terrace has a different surface morphology indicates that it is not the same Bi_2 adlayer on Bi_2Te_3. Moreover, the surface morphology of the lower terraces with shallow holes also appears different to that of pristine Bi_2Te_3, suggesting that this may be a different Bi-rich structure, which has not been identified in previous reports.[14,15] Further evidence that these terraces are not pristine Bi_2Te_3 comes from observation of reactions with Mn, which is discussed next and possible structures are discussed below based on DFT results.

2.2. Surface Reaction with Deposited Mn

MnBi alloys are promising ferromagnetic materials[16,20] and the self-formation of a stable bismuthene layer at the surface of Bi_2Te_3 may provide a template for the formation of a 2D MnBi alloy be reacting the bismuthene layer with Mn. To investigate the possibility of such a 2D alloy formation, we deposited close to a monolayer amount of Mn at a sample temperature of 15 °C. We selected a temperature below the tellurium desorption so that tellurium atoms from the bulk have minimal effect on the reaction. We deposited Mn atoms on the sample shown in Figure 2c (sample containing bismuth bilayer islands). After reaction with Mn, the surface morphology changes, and the edges of the irregular islands develop preferred crystallographic orientations, causing the smooth edges to exhibit short segments of straight edges, as shown in the large-scale STM topography in **Figure** 3a. The shape of the edge indicates a stronger crystallographic anisotropy of the edge energies, suggesting the formation of a new alloy phase. One small, almost triangular-shaped island was observed, which is indicated by a black arrow in Figure 3a. The line profile in blue color in Figure 3a shows that the thickness of the islands slightly increased compared to Bi_2 and now measures ≈0.4–0.5 nm. In addition, some sections along the edges have a slightly larger contrast, as apparent in Figure 3b, which may indicate some compositional variation of these regions along the edges. Surprisingly, after reaction with Mn, both the islands and terraces in between the islands exhibit very similar surface morphologies, suggesting transformation to a similar alloy. Both terraces show small domains with contrast variation of 0.1–0.2 nm, which is more evident when zoomed in, as shown in Figure 3b. The red line profile on the top layer shows that the depression ranges from 0.1 to 0.2 nm. Likewise, the green line profile in the bottom layer also shows similar depressions in random shape. Both the modified bismuth bilayer islands and bottom layer show hexagonal atomic arrangement, as shown in Figure 3c,d.

XPS analysis before and after the reaction of the surface with Mn is shown in **Figure** 4. Reaction with Mn causes a small (≈0.2 eV) shift of the Bi-4f peak to lower binding energy while Te remains unchanged. The Mn-2p peak exhibits a shake-up

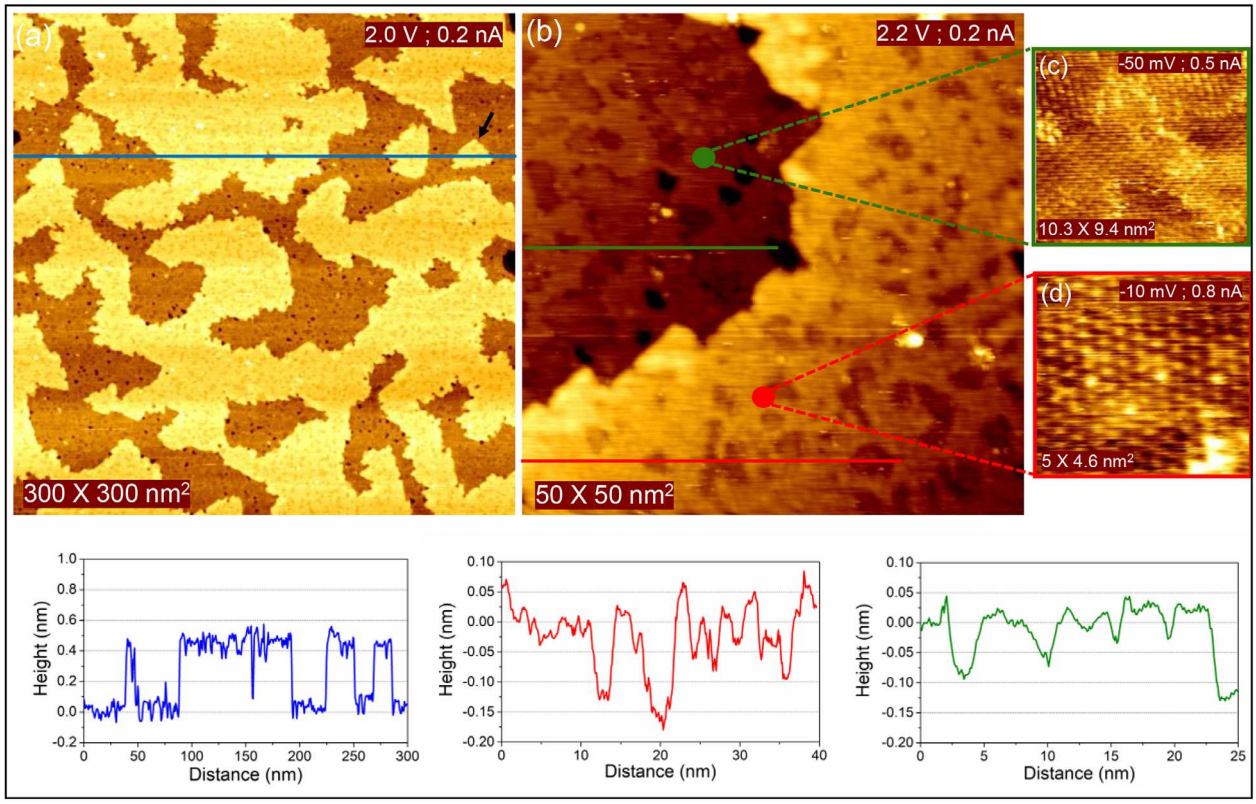

Figure 3. STM characterization of the morphology after Mn-deposition and reaction. a) The large-scale topography shows that the edges of bismuth bilayer islands have modified and become zigzag-shaped. One triangular island, denoted with a black arrow, is observed, suggesting stronger anisotropy in the step-edge energies of the alloyed terraces. The blue line profile shows the terrace height of ≈0.4–0.5 nm. Small height variations are observed throughout the surface. b) These height variations are clearer when zoomed in. The red line profile on the top layer shows the height variations in the range of 0.1–0.2 nm. The top and bottom terraces exhibit similar morphologies with a hexagonal atomic arrangement c,d).

satellite characteristic for Mn^{2+} charge state as shown in Figure 4e. The peak positions are denoted in Table S2 (Supporting Information). A shift to a lower binding energy of the Bi peak is consistent with electron transfer from Mn to Bi. However, it is unclear if this charge transfer occurs to the Bi_2 layer or the substrate, since the probing depth in XPS is several nanometers.

The similar reaction of Mn with the Bi_2-islands and the lower terrace may suggest similarities in their respective composition despite their different appearances in STM (Figure 2c). Specifically, it questions the assertion that the lower terraces may be Bi_2Te_3 layers. To verify that Bi_2Te_3 reacts differently with Mn, we deposited a similar amount of Mn vapor at 150 °C on pristine Bi_2Te_3 crystal, a sample akin to that shown in Figure 2b. **Figure** 5a shows a clean Bi_2Te_3 sample before Mn deposition. Small clusters appear on the STM morphology after Mn evaporation, as shown in Figure 5b. We use the same size (50 × 50 nm^2) of the STM image for better comparison with the pristine sample. The step height (1 nm) of Bi_2Te_3 remains the same, as indicated in the line profile in Figure 5c. The cluster heights vary from 0.3 to 1 nm, as shown in the line profiles in Figure 5.

XPS measurements, shown in **Figure** 6a, show that Mn is in a 2+ charge state, while there is very little change in the Bi-4f and Te-3d core levels before and after Mn deposition, as shown in Figure 6a. Low energy ion scattering spectroscopy (LEIS), shown in Figure 6b, exhibits an intense peak at ≈900 eV, corresponding to Mn atoms, and also indicates that Mn is at the surface after deposition at 150 °C. The peaks at ≈1035 and ≈1070 eV are related to Te and Bi atoms, respectively. The Mn charge state suggests that Mn reacts with tellurium from Bi_2Te_3 and forms MnTe clusters at the surface. Stepwise annealing to 300 °C causes a gradual decrease of both the Mn-2p intensity in XPS as well as the Mn-peak in LEIS. This result is consistent with either the formation of larger MnTe clusters on the surface or the diffusion of Mn into the bulk.

So far, from our discussions, it is apparent that the reaction of Mn with pristine Bi_2Te_3 is different to that of the terraces in between Bi_2 islands. This suggests that these terraces are not Bi_2Te_3 but have a different composition. Such a surface should be close to equilibrium with Bi_2 and thus in a Bi-rich environment. To investigate possible surface structures for such conditions, we performed DFT simulations to find phases that are consistent with the experiment. Furthermore, we investigated possible compounds that would form by reacting these surface phases with Mn.

2.3. DFT-Calculations

To assess potential Bi-rich surface phases, the energetics of different compositional Bi-Te phases constructed by removal of Te

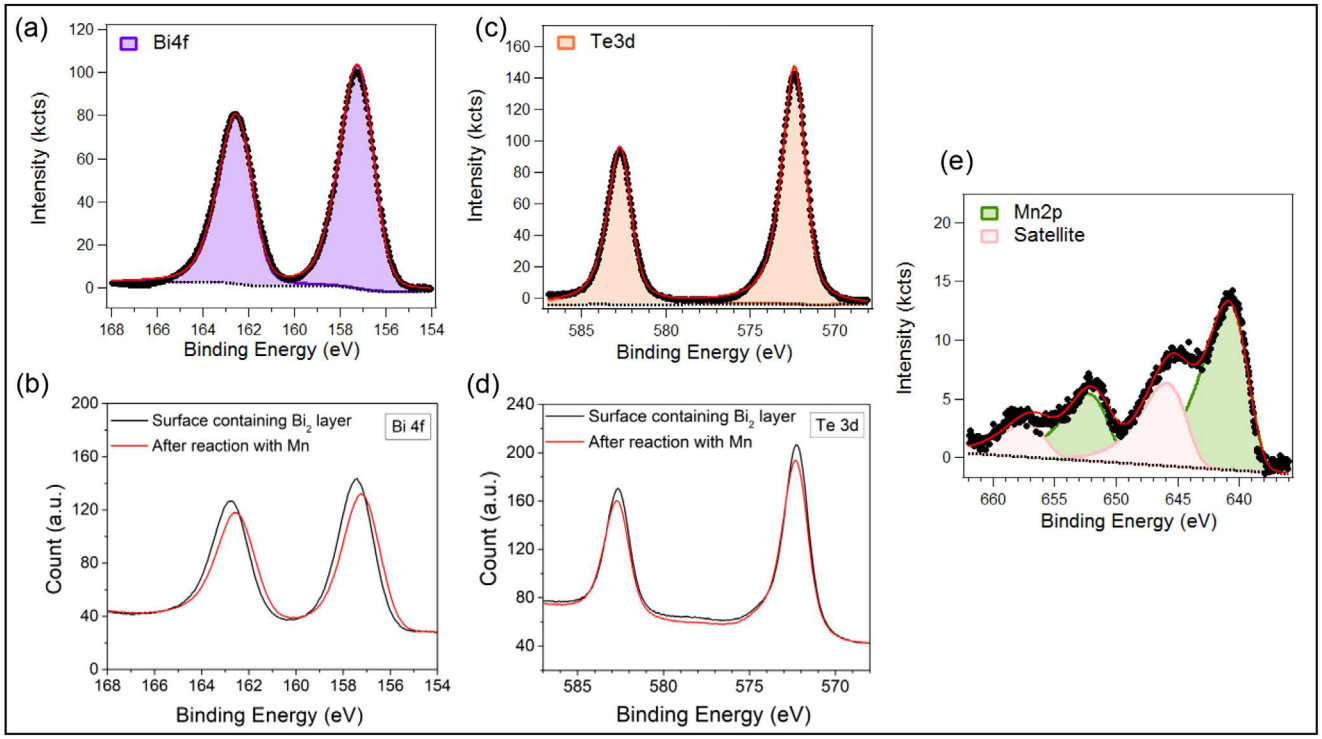

Figure 4. XPS analysis of Mn reaction with a Bi-rich Bi_2Te_3 surface. a) Bi-4f core level spectra after reaction with Mn vapor at 150 °C substrate temperature. b) A comparison of Bi-4f XPS spectra before and after Mn evaporation shows a clear shift in peak position. c) Te-3d XPS spectra after reaction with Mn vapor. d) The simultaneous plot shows a negligible difference in the Te-3d core level after the reaction with Mn. e) Mn-2p core level spectra after deposition. Two satellite peaks are observed along with $2p_{3/2}$ and $2p_{1/2}$.

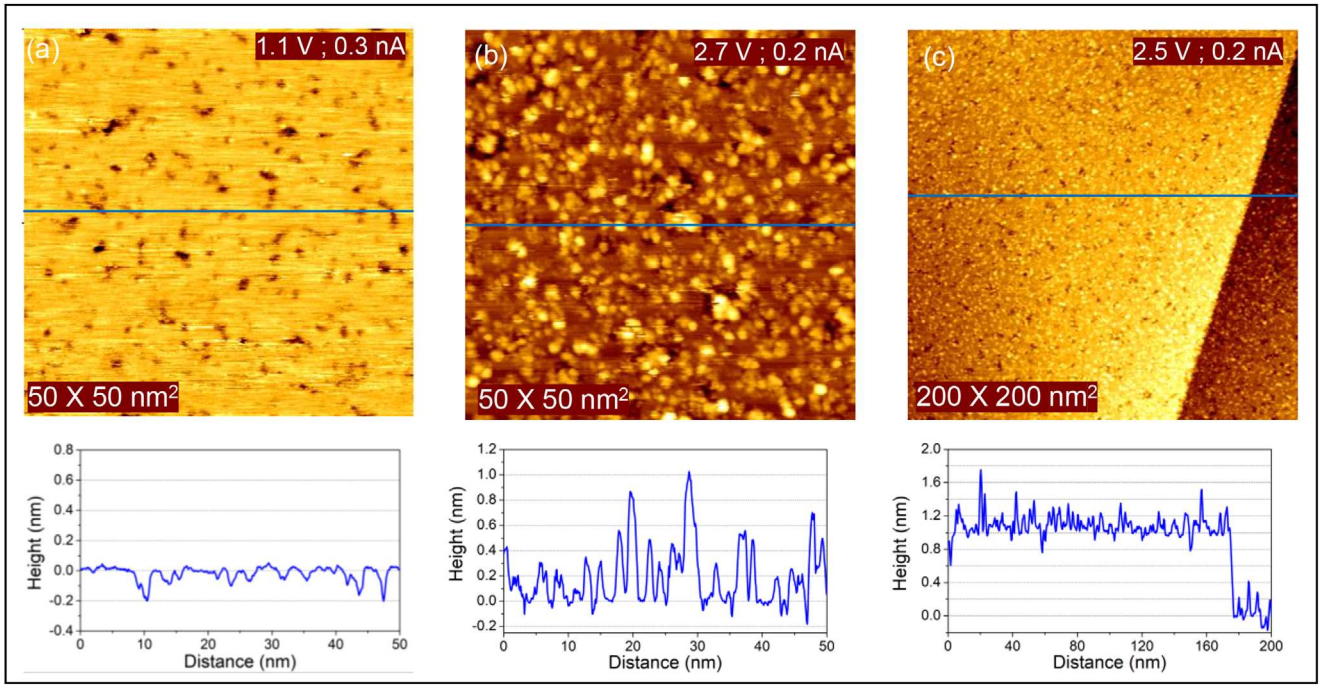

Figure 5. Surface morphology of the Bi_2Te_3 sample with Mn deposition at 150 °C. a) STM topography of a clean Bi_2Te_3 crystal. b) Small clusters appear throughout the surface after Mn evaporation. c) The line profile in large-scale STM topography shows that the QL thickness of Bi_2Te_3 remains intact at 1 nm. The sizes of the clusters are random, and the line profile shows that the thickness ranges from 0.3 to 1 nm.

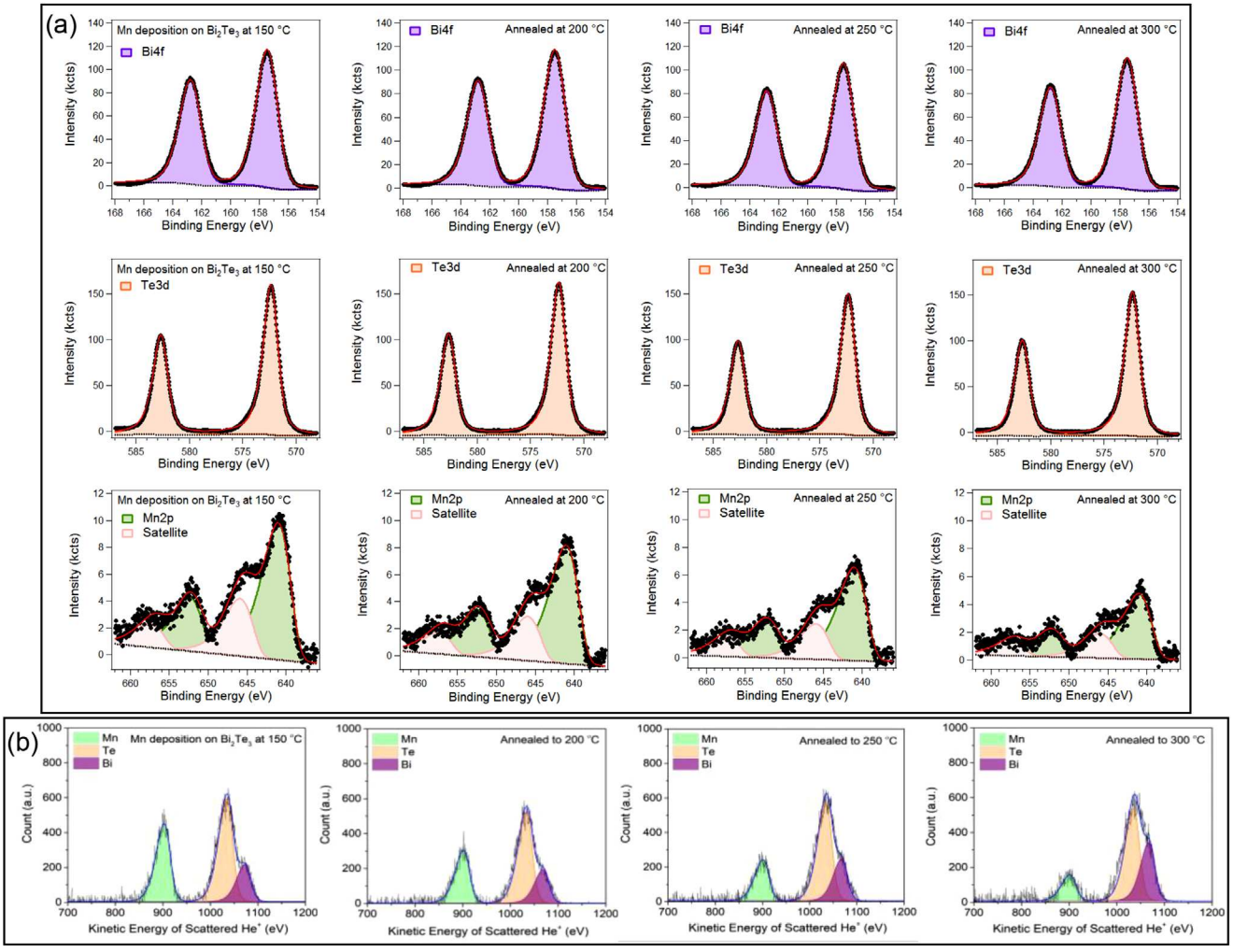

Figure 6. X-ray photoelectron spectroscopy (XPS) and low-energy ion scattering spectroscopy (LEIS) analysis of Mn deposition on Bi_2Te_3 at 150 °C and consecutive annealing steps. a) There is very little variation in Bi-4f and Te-3d core level spectra, Mn-2p shows satellite peaks suggesting a 2+ oxidation state. The intensity of Mn-2p drops gradually with the annealing temperature. b) LEIS spectra show three peaks corresponding to Mn, Te, and Bi atoms. The intense Mn peak after deposition denotes the presence of Mn on the surface layer. A systematic drop of both the Mn-2p intensity in XPS as well as the Mn-peak in LEIS suggests either the formation of larger MnTe clusters on the surface or the diffusion of Mn deep into the bulk.

layer(s) from the Bi_2Te_3 structure are evaluated. Panel **Figure** 7b shows the surface of Bi_2Te_3. We will denote the two surface quintuple layers as $Bi_4Te_{6,}$ as indicated in Figure 7b. It can be labeled as TBTBT-TBTBT, where T(B) stands for Te(Bi) layer. Next, we remove the surface Te layer from Bi_4Te_6, which results in the following surface structure BTBT-TBTBT. In the same way, we remove single Te layers from different positions within surface Bi_4Te_6, resulting in five more surface structures. Some examples are TBBT-TBTBT and TBTB-TBTBT. This family of structures is denoted as Bi_4Te_5. All structures in the family are subjected to structural relaxation, their energies are calculated, and the lowest energy structure is retained. Next, the same strategy is applied for removing two Te layers, which results in the family of surface structures Bi_4Te_4. The family of surface structures that results from removing three Te layers is denoted as Bi_4Te_3. Some members from this family are shown in Figure 7b and correspond to TBTBT-BB and BB-TBTBT surface structures. A similar strategy is applied to produce structures in the Bi_4Te_2 and Bi_4Te families. In each of the families we retain the lowest energy structure. They are TBTB-TBTBT, TBTBT-BBT, TBTBT-BB, BB-BTBT, and BB-TBB for Bi_4Te_5, Bi_4Te_4, Bi_4Te_3, $Bi_4Te_{2,}$ and Bi_4Te_1, respectively. The structures are visualized and their energies are reported in Figures S4–S7 (Supporting Information). They are provided in ref. [25].

These structures have a different number of Te atoms and therefore grand potential is the appropriate thermodynamic function to predict their relative stability. The grand potential is:

$$\Omega = E\ (NBi, NTe) - TS - NBi\mu Bi - NTe\mu Te \quad (1)$$

where, E (N_{Bi}, N_{Te}) is the internal energy of the slab, N_{Bi} and N_{Te} is the number of Bi and Te atoms, respectively, μ_{Bi} and μ_{Te} is the chemical potential for Bi and Te, respectively, T and S are the temperature and entropy, respectively. In crystalline solids, the differences in internal energy (first term in Equation (1)) between different structures are typically much larger than the

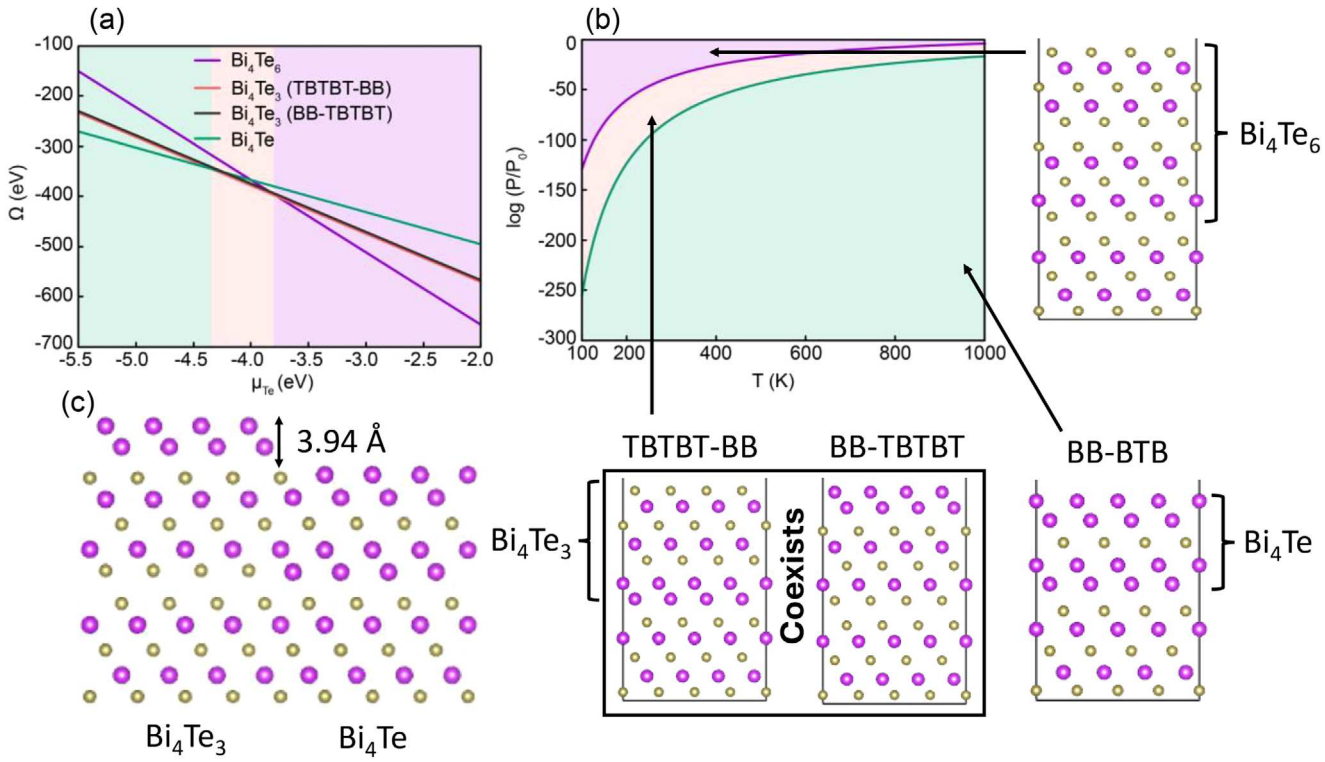

Figure 7. a) Grand potential for Bi_xTe_y phases. b) The phase diagram for Bi_xTe_y surface structures and their visualization. c) The schematic representation for Bi_4Te_3 and Bi_4Te surface structure coexistence.

entropic (second term in Equation (1)) differences between the structures.[26] Therefore, we can treat the entropic contributions in Equation (1) as being approximately constant for all the structures we consider. Furthermore, all structures have the same number of Bi atoms therefore the third term of Equation (1) is also constant for all the structures. Since our goal is to compare Ω for different structures these constant terms can be neglected. We compute Ω for the lowest energy structures from each family Bi_xTe_y and give the data for those that minimize Ω in Figure 7a. Note that we also included BB-TBTBT structure from Bi_4Te_3 family since it is very competitive with TBTBT-BB in both energy and grand potential and also experimentally relevant. The point where $\Omega(\mu_{Te})$ for different structures cross is the phase coexistence point. Figure 7a reveals two points of phase coexistence: between Bi_4Te_6 and Bi_4Te_3 at a higher value of chemical potential ($\mu^{coex} = -3.79$ eV) and between Bi_4Te_3 and Bi_4Te_1 at a lower value of chemical potential ($\mu^{coex} = -4.32$ eV). They can now be used to obtain phase diagram for Bi_xTe_y. If we treat Te vapor as an ideal gas, its chemical potential can be written as $\mu_{Te} = k_B T \ln \frac{P}{k_B T n_Q}$, where P is pressure; $n_Q = \left(\frac{m_{Te} k_B T}{2\pi\hbar^2}\right)^{3/2}$, and m_{Te} is the mass of Te atom. This equation can be used to produce phase coexistence lines, P(T), from μ^{coex}, which separate different phases of Bi_xTe_y. The data are given in Figure 7b and predict the following sequence of surface transformations as the temperature increases at constant pressure: $Bi_2Te_3 \rightarrow Bi_4Te_3$ (TBTBT-BB or BB-TBTBT) $\rightarrow Bi_4Te$ (BB-TBB). This prediction is in agreement with experimental findings that as annealing temperature increases, Te leaves the surface causing its transformation into Bi-rich surfaces. Experimentally, two different regions are present (see Figure 2c). Since experimental conditions are nonequilibrium we propose that the two regions correspond to the coexisting of Bi_4Te_3 and Bi_4Te structures at the surface: BB-TBTBT and BB-TBB. Such nonequilibrium structure is schematically shown in Figure 7c. Interestingly the step height of 3.94 Å matches well experimental step height of 4.0 Å.

Next, we investigate interaction of BB-TBTBT and BB-TBB surface structures with Mn. We simulate one layer of Mn introduced in different locations within the three top atomic layers of Bi_xTe_y as shown in **Figure 8** (side view) and Figure S8 (Supporting Information) (top view). Structures are subjected to relaxation in both ferromagnetic and antiferromagnetic configurations as visualized in Figure 8 and Figure S8 (Supporting Information). We find that the surface structures with Mn layer in between Bi and Te are the most favorable for both Bi_4Te_3 and Bi_4Te structures. This can be attributed to the stronger bond between Mn and Te as compared to Mn and Bi. For example, the bond lengths for Mn-Te and Mn-Bi are 2.72 and 3.48 Å, respectively. Interestingly, we find that despite a chemically rather similar environment for the Mn layer in the two lowest energy structures in Figure 8a,g, their magnetic ordering is different. In particular, Bi_4Te_3 and Bi_4Te exhibit ferromagnetic and antiferromagnetic order, respectively. Interestingly, the intercalated Mn layer is a rare example of a triangular 2D Ising model, which is known to be analytically solvable. The transition between paramagnetic and ferromagnetic configuration occurs at $J/k_BT_C = 0.2747$, where J is the exchange constant expressed in energy units and T_C is the Curie point.[27] The exchange constant is the difference between the energies per

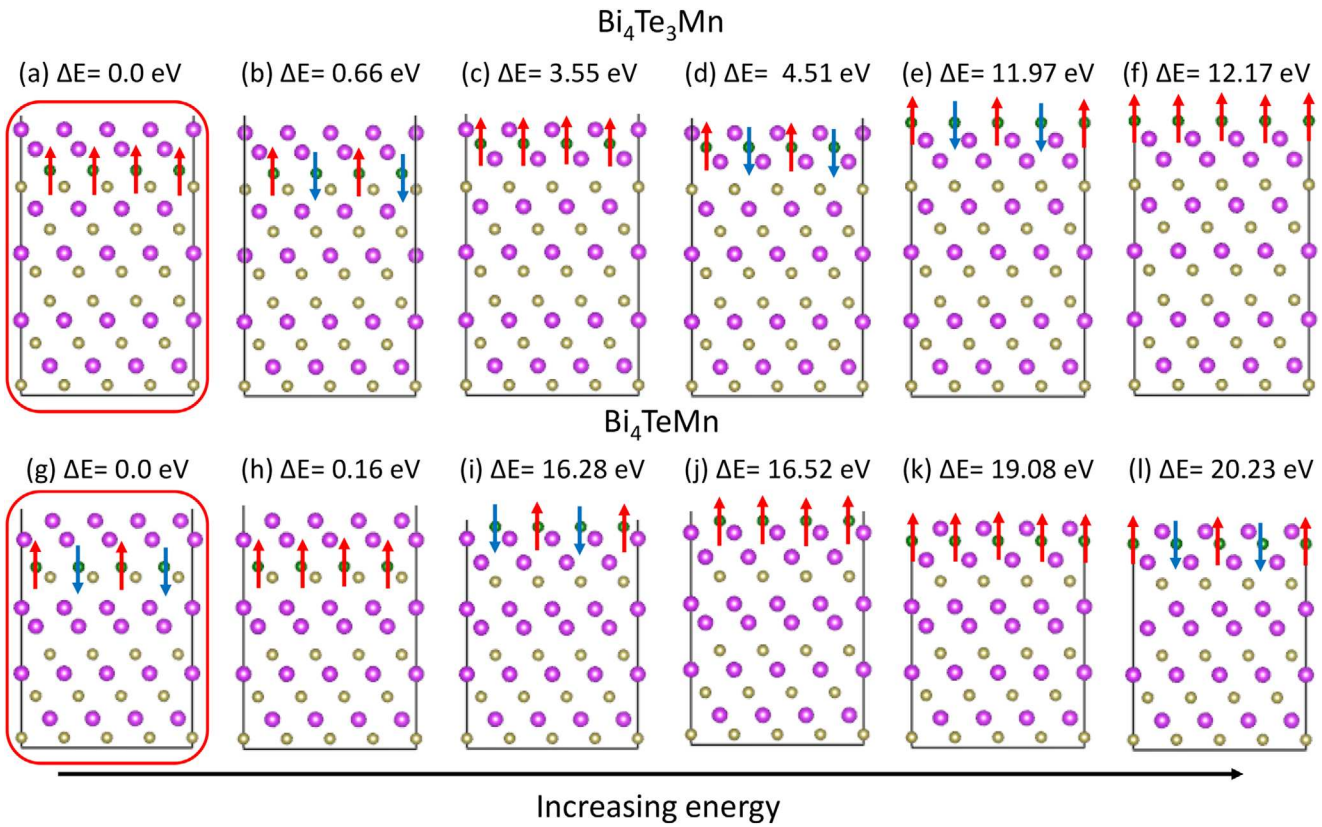

Figure 8. Visualization of Bi_4Te_3Mn a–f) and Bi_4TeMn g–l) supercells and magnetic moments on Mn. Structures are ordered according to the energy increase.

magnetic ion of antiferromagnetic and ferromagnetic configurations. The exchange constants for Bi_4Te_3Mn and Bi_4TeMn are 4.17 and −9.67 meV, respectively. Thus, the Curie temperature associated with a ferromagnetic transition in Bi_4Te_3Mn is 176 K. We are not aware of an analytical result for the antiferromagnetic transition temperature in a 2D magnetic system. However, given that the exchange constant for Bi_4TeMn is about twice that for Bi_4Te_3Mn we can speculate that antiferromagnetic transition will occur at higher temperatures as compared to the ferromagnetic one.

3. Conclusion

Annealing of Bi_2Te_3 in vacuum causes the loss of Te. The remaining Bi-rich surface rearranges to form stable Bi_2 layers. In addition to previously considered Bi_2 layers on top of Bi_2Te_3 substrates, our DFT calculations suggest the presence of other Bi-rich phases, particularly a phase consisting of two Bi_2 layers separated by a single Te-layer. These phases may co-exist at low Te chemical potential and thus explain the experimental observations of two co-existing surface terminations. The similarity between these two surfaces may also explain their comparable reactions with Mn. This makes this a potentially interesting surface alloy for inducing properties into the underlying TI by proximity. While we initially anticipated that the reaction of Bi_2 surface layers with Mn may cause the formation of a MnBi alloy layer, DFT calculations suggest that the Mn-Te affinity causes the deposited Mn to diffuse through the Bi-layer and adsorb on the Te. The uniform adsorption of Mn between Te- and Bi-layer is consistent with the STM images that indicate a planar structure after reaction with Mn. Such an adsorption of Mn on the Te-layer is, however, in contrast to the adsorption of Mn directly on Bi_2Te_3, which causes the extraction of Te and formation of disordered MnTe clusters. This implies that the Bi_2 layer on top stabilizes the Mn-monolayer and suppresses the formation of clusters. One motivation for the formation of MnBi monolayer alloys was the attempt to interface an ultrathin ferromagnetic alloy layer with a topological insulator. While the MnBi alloy layer may not form, XPS shows that Mn has a 2+ charge and thus is in a high-spin state. DFT also suggests a ferromagnetic or antiferromagnetic ordering for the two surface structures, respectively. This should motivate future experimental studies on the characterization of the magnetic properties of these heterostructures.

4. Experimental Section

The Bi_2Te_3 single crystal was mechanically exfoliated in air and immediately put inside a UHV chamber. The sample was degassed initially at 150 °C, then stepwise vacuum annealed at 200 and 300 °C. Manganese was evaporated from a water-cooled mini e-beam evaporator. A home-built Ta-crucible was used to contain Mn flakes. Mn deposition was calibrated by intercalation experiments in bilayer VSe2 where well-ordered structures with defined Mn amounts are formed.[10] A monolayer of Mn was defined as one Mn-atom per Bi2Te3 unit cell, or ≈6 atoms nm^{-2}.

To confirm the amount of Mn the XPS intensity of the Mn-2p peak was compared for different samples. Mn was evaporated at a substrate temperature of 150 °C. The prepared samples are transferred to the surface science analysis chamber without breaking the vacuum to perform STM, XPS, and LEIS measurements. The STM measurements are performed with an Omicron VT-STM operated at room temperature. The STM tips are fabricated with etched tungsten wires and cleaned by voltage pulsing. For XPS studies, a non-monochromatized dual anode X-ray (Mg-K_α) source was used for photoexcitation, and an Omicron Sphera hemispherical analyzer was employed for photoelectron detection. The binding energy (284.8 eV) of the C-1s peak from "adventitious carbon" was used as a reference for calibration. The data collection of low-energy ion scattering spectroscopy was performed with a differentially pumped focused extractor noble gas ion source (SPECS IQE 12/38). The energy of incident He^+ ions was 1200 eV, and the scattering angle was fixed at 1300°. The same electrostatic hemispherical analyzer (Omicron Sphera Analyzer) as for XPS was used with reversed polarity to detect scattered He^+ ions.

Computational Section: To simulate Bi_2Te_3 surfaces the first-principles DFT calculations were used as implemented in Vienna ab initio simulation package (VASP).[28,29] The electron-ion interactions of the system were described by projector augmented-wave (PAW) potentials.[30,31] Perdew–Burke–Ernzerhof (PBE)[32] for exchange and correlation potential in the generalized gradient approximation (GGA) were adopted for all the calculations along with D3 dispersion corrections as proposed by Grimme et al.[33] For the Brillouin zone integration, a Monkhorst–Pack k-space mesh in reciprocal space was used with the spacing between k-points of 0.22 $Å^{-1}$. The plane wave basis cutoff energy was 600 eV. The slabs are simulated using a supercell that contains 4 × 4 × 1 unit cells of Bi_2Te_3 (see Figure S3b, Supporting Information). Periodic boundary conditions are applied along all three Cartesian directions and the vacuum layer of 35 Å introduced to separate images along the growth directions. The supercell contains three quintuple layers of Bi_2Te_3 along the growth direction. The in-plane lattice constants were fixed to their bulk values. The out-of-plane lattice constant was fixed to the value 64.8 Å. Furthermore, the ionic positions of the bottom quintuple layer are kept fixed to simulate surface rather than slab geometry. The ionic positions in the rest of the layers were relaxed until forces on all atoms were less than 1 meV $Å^{-1}$. For magnetic calculations, the on-site Coulomb interaction was accounted using a Hubbard-like effective U parameter[34] (with U = 4 eV) for Mn 3d states.

Supporting Information

Supporting Information is available from the Wiley Online Library or from the author.

Acknowledgements

The experimental group acknowledges support from the NSF under grant DMR 2118414. The theory group acknowledges support from the U.S. Department of Energy, Office of Basic Energy Sciences, Division of Materials Sciences and Engineering under Grant No. DE-SC0005245. Computational support was provided by the National Energy Research Scientific Computing Center (NERSC), a U.S. Department of Energy, Office of Science User Facility located at Lawrence Berkeley National Laboratory, operated under Contract No. DE-AC02- 05CH11231 using NERSC Award No. BES-ERCAP-0025236.

Conflict of Interest

The authors declare no conflict of interest.

Data Availability Statement

The data that support the findings of this study are available from the corresponding author upon reasonable request.

Keywords

2D materials, bismuthene, magnetic interfaces, MnBi alloy, surface alloys, topological insulator, topotaxy

Received: April 17, 2025
Revised: July 21, 2025
Published online: August 13, 2025

[1] X. L. Qi, S. C. Zhang, *Rev. Mod. Phys.* **2011**, *83*, 1057.
[2] M. Z. Hasan, C. L. Kane, *Rev. Mod. Phys.* **2010**, *82*, 3045.
[3] Y. Xia, D. Qian, D. Hsieh, L. Wray, A. Pal, H. Lin, A. Bansil, D. Grauer, Y. S. Hor, R. J. Cava, M. Z. Hasan, *Nat. Phys.* **2009**, *5*, 398.
[4] H. J. von Bardeleben, J. L. Cantin, D. M. Zhang, A. Richardella, D. W. Rench, N. Samarth, J. A. Borchers, *Phys. Rev. B.* **2013**, *88*, 075149.
[5] P. P. J. Haazen, J. B. Laloë, T. J. Nummy, H. J. M. Swagten, P. Jarillo-Herrero, D. Heiman, J. S. Moodera, *Appl. Phys. Lett.* **2012**, *100*, 082404.
[6] C. Z. Chang, P. Tang, Y. L. Wang, X. Feng, K. Li, Z. Zhang, Y. Wang, L. L. Wang, X. Chen, C. Liu, W. Duan, K. He, X. C. Ma, Q. K. Xue, *Phys. Rev. Lett.* **2014**, *112*, 056801.
[7] M. Mogi, T. Nakajima, V. Ukleev, A. Tsukazaki, R. Yoshimi, M. Kawamura, K. S. Takahashi, T. Hanashima, K. Kakurai, T.-h. Arima, M. Kawasaki, Y. Tokura, *Phys. Rev. Lett.* **2019**, *123*, 016804.
[8] S. Khatun, O. Alanwoko, V. Pathirage, C. C. de Oliveira, R. M. Tromer, P. A. S. Autreto, D. S. Galvao, M. Batzill, *Adv. Funct. Mater.* **2024**, *34*, 2315112.
[9] V. Pathirage, S. Khatun, M. Batzill, *Surf. Sci.* **2025**, *754*, 122695.
[10] V. Pathirage, S. Khatun, S. Lisenkov, K. Lasek, J. F. Li, S. Kolekar, M. Valvidares, P. Gargiani, Y. Xin, I. Ponomareva, M. Batzill, *Nano Lett.* **2023**, *23*, 9579.
[11] K. Lasek, J. F. Li, M. Ghorbani-Asl, S. Khatun, O. Alanwoko, V. Pathirage, A. V. Krasheninnikov, M. Batzill, *Nano Lett.* **2022**, *22*, 9571.
[12] J. W. G. Bos, H. W. Zandbergen, M. H. Lee, N. P. Ong, R. J. Cava, *Phys. Rev. B.* **2007**, *75*, 195203.
[13] M. Chen, J. P. Peng, H. M. Zhang, L. L. Wang, K. He, X. C. Ma, Q. K. Xue, *Appl. Phys. Lett.* **2012**, *101*, 081603.
[14] I. I. Klimovskikh, D. Sostina, A. Petukhov, A. G. Rybkin, S. V. Eremeev, E. V. Chulkov, O. E. Tereshchenko, K. A. Kokh, A. M. Shikin, *Sci. Rep.* **2017**, *7*, 45797.
[15] P. M. Coelho, G. A. S. Ribeiro, A. Malachias, V. L. Pimentel, W. S. Silva, D. D. Reis, M. S. C. Mazzoni, R. Magalhaes-Paniago, *Nano Lett.* **2013**, *13*, 4517.
[16] M. C. J. Marker, P. Terzieff, P. Kainzbauer, M. Bobnar, K. W. Richter, H. Ipser, *J. Alloys Compd.* **2018**, *741*, 682.
[17] M. J. Kramer, R. W. McCallum, I. A. Anderson, S. Constantinides, *JOM* **2012**, *64*, 752.
[18] T. Roman, I. I. Murgulescu, G. Ababei, G. Stoian, M. Lostun, M. Porcescu, M. Grigoras, N. Lupu, *Mater. Today Commun.* **2022**, *33*, 104241.
[19] A. Sarkar, A. B. Mallick, *JOM* **2020**, *72*, 2812.
[20] Y. K. He, J. Gayles, M. Y. Yao, T. Helm, T. Reimann, V. N. Strocov, W. Schnelle, M. Nicklas, Y. Sun, G. H. Fecher, C. Felser, *Nat. Commun.* **2021**, *12*, 4576.
[21] X. Qin, L. Di, C. Sui, R. Zhao, J. Fan, F. Wang, X. Xu, *J. Alloys Compd.* **2020**, *842*, 155694.
[22] T. Hozumi, P. LeClair, G. Mankey, C. Mewes, H. Sepehri-Amin, K. Hono, T. Suzuki, *J. Appl. Phys.* **2014**, *115*, 17A737.
[23] U. Deffke, G. Ctistis, J. J. Paggel, P. Fumagalli, U. Bloeck, M. Giersig, *J. Appl. Phys.* **2004**, *96*, 3972.
[24] F. Reis, G. Li, L. Dudy, M. Bauernfeind, S. Glass, W. Hanke, R. Thomale, J. Schafer, R. Claessen, *Science* **2017**, *357*, 287.

[25] S. Lisenkov, USFmatscilab/BiTe, https://github.com/USFmatscilab/BiTe/tree/main.
[26] D. S. Sholl, J. A. Steckel, Density Functional Theory: A Practical Introduction, John Wiley& Sons, Inc, New Jersey, Hoboken, **2009**, pp. 83–112.
[27] R. J. Baxter, *Exactly Solved Models in Statistical Mechanics*, Elsevier, Amsterdam, Netherlands, **2016**.
[28] G. Kresse, J. Furthmuller, *Phys. Rev. B.* **1996**, *54*, 11169.
[29] G. Kresse, J. Furthmuller, *Comput. Mater. Sci.* **1996**, *6*, 15.
[30] P. E. Blochl, *Phys. Rev. B.* **1994**, *50*, 17953.
[31] G. Kresse, D. Joubert, *Phys. Rev. B.* **1999**, *59*, 1758.
[32] J. P. Perdew, K. Burke, M. Ernzerhof, *Phys. Rev. Lett.* **1996**, *77*, 3865.
[33] S. Grimme, *J. Comput. Chem.* **2006**, *27*, 1787.
[34] S. L. Dudarev, G. A. Botton, S. Y. Savrasov, C. J. Humphreys, A. P. Sutton, *Phys. Rev. B.* **1998**, *57*, 1505.